Target-thickness-dependent electron emission from carbon foils bombarded with swift highly charged heavy ions

Hermann Rothard, Christophe Caraby, Amine Cassimi, Benoit Gervais, Jean-Pierre Grandin, Pascal Jardin, and Matthias Jung

Centre Interdisciplinaire de Recherches avec les Ions Lourds, Laboratoire Mixte CEA-CNRS, CIRIL Boîte Postale 5133, Rue Claude Bloch, F-14040 Caen Cedex, France

Annick Billebaud and Michel Chevallier

Institut de Physique Nucléaire de Lyon, IN2P3-CNRS/Université Claude Bernard (Lyon I), 43 Boulevard du 11 Novembre 1918, F-69622 Villeurbanne Cedex, France

Karl-Ontjes Groeneveld and Robert Maier

Institut für Kernphysik der J. W. Goethe Universität, August-Euler-Strasse 6, D-60486 Frankfurt am Main, Germany

(Received 1 August 1994)

We have measured electron yields from the beam entrance and exit surfaces of thin carbon foils ($d \approx 4-700$ $\mu g/cm^2$) bombarded with swift (13.6 MeV/u) highly charged ($q = 16-18$) argon ions. The dependence of the electron yields on target thickness and charge state of the ions is analyzed within the framework of an extended semiempirical model. Due to the high velocity of the ions, it is possible to distinguish electron production in primary ionization (related to the stopping power and the effective charge of the ions) from secondary electron production due to the transport of so-called δ electrons (cascade multiplication). By combining the experimental results with numerical simulations of electron transport in matter by a Monte Carlo method, we have obtained electron transport lengths of high energy ($E \gg 100$ eV) δ electrons parallel and perpendicular to the ion trajectory, as well as diffusion lengths of slow electrons ($E \ll 100$ eV). In order to study the velocity dependence of these transport lengths, we have not only investigated 13.6 MeV/u Ar ions, but also 1 MeV/u C and 3.9 MeV/u S, for which experimental results are available [Koschar *et al.*, Phys. Rev. A **40**, 3632 (1989)]. We discuss the origin of electron yield reductions (compared to a simple scaling with the square of the nuclear charge) with heavy ions and present measurements of double differential energy and angular electron distributions of 13.6 MeV/u Ar^{17+} ions.

PACS number(s): 79.20.Rf, 34.90.+q

I. INTRODUCTION

Swift charged particles interact with matter mainly by electronic processes such as *excitation* and *ionization* of the target atoms. Positively charged projectiles may also *capture* target electrons (to the ground state or an excited state). If the projectiles carry electrons, electron *loss* or projectile excitation may take place. All of these processes contribute to the loss of kinetic energy of the projectile and the deposition of energy in matter, but most of the projectile energy loss per unit path length leads to ionization. Subsequent electron emission (EE) from the solid surface, the so-called *kinetic electron emission,* has first been described nearly a hundred years ago [1].

Electron production occurs whenever ionizing radiation interacts with matter. Consequently, the knowledge of the number of electrons emitted per incoming projectile (the electron *yield* γ) as well as their angular and energy distribution is needed in a variety of applications involving charged particles and, in particular, heavy ions. To give a few examples, we mention *particle track formation,* single-event-upset in electronic devices in spacecraft, and *radiation biology* and medicine (tumor treatment). An overview of applied aspects of EE has been given by Hasselkamp in Ref. [3]. Extensive recent reviews on EE from solids can be found in Refs. [2–4], and recent developments concerning fundamental and applied aspects of heavy ion physics can be found in Ref. [5].

A multitude of experiments have been performed on EE induced by slow or medium velocity heavy ions ($E_p < 1$ MeV/u) [3], but only a few studies with fast heavy ions have been published [6–12]. One can distinguish between two different types of experiments: studies of electron emission yields γ [10–12], or measurements of doubly differential electron energy spectra $d^2\gamma(\theta)/dEd\Omega$ as a function of the observation angle θ [6–9]. No systematic studies have been published for heavy ions ($Z > 8$) at energies above 10 MeV/u. Therefore, we have measured electron yields from the beam entrance and exit surfaces of thin carbon foils ($d \approx 4-700$ $\mu g/cm^2$) bombarded with swift ($E_P = 13.6$ MeV/u, $v_P \approx 23$ a.u.) highly charged ($q = 16-18$) argon ions. Since about 80–95 % of all emitted electrons are of low energy ($E \ll 100$ eV) [3], electron yield measurements provide us with information about these low-energy electrons, whereas electron spectra yield information on high-energy electrons ($E > 100$ eV). Following Sternglass [13], we will refer to this high-energy part as "δ *electrons.*" In contrast, we will not use the term "*secondary electrons*" for the low-energy part, because

low-energy electrons are not only produced in secondary collision processes, an important fraction is produced in direct primary ionization events.

In the following Sec. II, we describe an extended semiempirical model for EE. The Monte Carlo (MC) simulations of electron transport in carbon are the subject of Sec. III. After a short description of the experimental setup (Sec. IV), we present the experimental results. They will be analyzed within the framework of the semiempirical model (Sec. V). Electron transport lengths are obtained by combining these results with the MC studies (Sec. VI). We finally investigate the question of scaling of the electron yields with the projectile energy loss (Sec. VII), and present double differential electron spectra as an outlook in Sec. VIII.

II. SEMIEMPIRICAL MODEL

We will now describe an extension of the semiempirical theory of EE introduced by Sternglass [13]. The basic idea of this simple approach is illustrated in Fig. 1. Usually, electron emission is regarded as a three-step process: *production* of electrons by primary ionization, *transport* of the electrons through the solid including secondary electron production by fast electrons (cascade multiplication) and, finally, *transmission* through the surface and ejection into the vacuum.

Electron emission yields are expected to be (roughly) proportional to the electronic energy loss per unit path lengths dE/dx [2–4,12–14]. Sternglass [13] and Koschar *et al.* [12] started from this assumption by further considering that projectile kinetic energy may be lost in two different types of collision processes: violent binary *close collisions* with a small projectile-target electron impact parameter, and *soft collisions* with a large impact parameter. This concept is discussed in two classical papers by Bohr and Lindhard and Winther [15]. Koschar *et al.* [12] introduced the so-called "partition factor" β_δ describing the fraction of projectile energy lost in close collisions with subsequent δ-electron emission. The fraction dissipated in soft collisions, leading to direct production of low-energy electrons (or to plasmon creation with subsequent electron production by plasmon decay), is given by $\beta_S=(1-\beta_\delta)$. Sternglass [13] assumed an equipartition between the two types of collision processes, i.e., $\beta_\delta=\beta_S=0.5$ for fast projectiles of velocities $v_P > Z_P^{2/3} v_0$ (with the Bohr velocity $v_0=1$ a.u.). In the present model, the dissipation of projectile energy in nonionizing events (e.g., target or projectile excitation with subsequent photon emissions, etc.) is neglected, and thus

$$\frac{dE}{dx}=\frac{dE}{dx}\bigg|_{\text{close}}+\frac{dE}{dx}\bigg|_{\text{soft}}=\beta_\delta\frac{dE}{dx}+\beta_S\frac{dE}{dx} . \tag{1}$$

In the following, we will establish simple equations for the target thickness dependence of forward and backward electron emission yields from thin foils [3,12,13]. We start by calculating the number N_{LE} of *low energy* electrons produced inside the solid by (1) *primary ionization in soft collisions* (denoted as "spi") and (2) *secondary ionization* by high-energy primary electrons from close collision (denoted by "δ"). Of course, there is no exact boundary between "low-energy" and "high-energy" (or, as we have decided to call them, δ) electrons. The "mean electron energy," defined as the first moment of the electron energy distribution, $\langle E\rangle=\int EN(E)dE/\int N(E)dE$ (integration from 0 to ∞), depends mainly on v_P, but also on Z_P and is in the order of some hundred eV. One may speak of *"slow"* or *"low energy"* electrons if their energy is $E \ll \langle E\rangle$ and consequently, of "fast" electrons if $E \gg \langle E\rangle$. As will become clear from Sec. IV, our experiment allows one to distinguish roughly between "slow" or "fast" electrons divided by a boundary situated somewhere between 100 eV and some hundred eV.

We assume that the direct *production* of low-energy electrons is proportional to the fraction of dE/dx dissipated in soft collisions. Furthermore, from now on, we assume that dE/dx varies only slowly with penetration depth. The number $dN_{\text{LE}}^{\text{spi}}$ of slow electrons from primary ionization by soft collisions (spi) in a layer dx at depth x is then given by

$$dN_{\text{LE}}^{\text{spi}}=\frac{\beta s}{\langle W\rangle}\frac{dE}{dx}dx , \tag{2}$$

where $\langle W\rangle$ denotes the mean energy transferred in an ionization event to liberate an electron. $\langle W\rangle$ is in the order of some ten eV.

The high-energy δ electrons will also produce low-energy electrons due to secondary ionization processes during their migration through the solid. The number $d^2N_{\text{LE}}^{\delta}$ of low-energy secondary electrons liberated in a layer dx at x by δ electrons produced in a layer dz at z is

$$d^2N_{\text{LE}}^{\delta}=\frac{\beta_\delta}{\langle W\rangle}\frac{dE}{dx}g(x-z)dx\,dz , \tag{3}$$

where $g(x-z)$ represents the spatial distribution of the energy carried away by the δ electrons originating in dz at z. For a target of infinite thickness, and this is the case considered in Sternglass' paper [13], we would obtain the total number dN_{LE}^{δ} of low-energy secondary electrons liberated in a layer dx at x by integrating Eq. (3) from 0 to

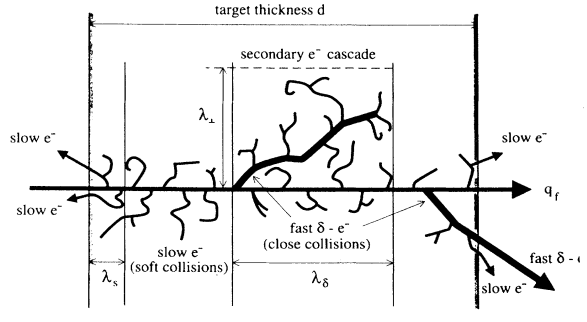

FIG. 1. Ionization of a solid by ions: basic concepts concerning the semiempirical model of electron emission involving electron transport lengths of high-energy δ electrons parallel (λ_δ) and perpendicular ($\lambda_\perp$) to the ion trajectory, and also diffusion lengths λ_S of slow "secondary" electrons ($E < 100$ eV).

∞ over dz. If we are interested in *thin foils* of *target thickness* d, the integration over dz has to be performed from 0 to d. For sufficiently thin targets, we can assume that dE/dx is constant for all z, and the integration results in

$$dN_{\mathrm{LE}}^{\delta}=\frac{\beta_{\delta}}{\langle W\rangle}\frac{dE}{dx}f(x,\lambda_{\delta})dx \tag{4}$$

with

$$f(x,\lambda_{\delta})=\int_0^d g(x-z)dz\ . \tag{5}$$

As shown by Sternglass in an appendix to his paper [13], the following simple form can be used for the transport function $f(x,\lambda_{\delta})$ in the case of low atomic number target materials under the assumption that $g(x-z)$ is the solution of the diffusion equation for a plane source:

$$f(x,\lambda_{\delta})=1-\exp\left[\frac{-x}{\lambda_{\delta}}\right]\ . \tag{6}$$

In this simple case, the transport of high-energy electrons is described by a characteristic mean transport length λ_{δ} for these δ electrons. Backscattering of δ electrons and thus contributions of layers dz at $z>x$ on low-energy electron production at $x<z$ has been neglected: in other words, Eq. (3) has only been integrated from 0 to x, and not from 0 to d.

In order to elucidate the meaning of λ_{δ}, we mention that in his original paper, Sternglass called $\lambda_{\delta}=(\frac{1}{3}R_{\delta}\lambda_{\tau})^{1/2}$ the "effective penetration distance" or "diffusion length of the delta rays" [13]. It is some averaged quantity containing both "the absorption mean-free path (which) is equal to the range R_{δ} of the δ rays measured along their track length" and the transport mean-free path λ_{τ}, i.e., the collision mean-free path projected on the beam direction.

Up to now, we treated the *production* of low-energy electrons by assuming that their number is proportional to the electronic energy loss per unit path length [Eqs. (2) and (3)]. The transport of high-energy electrons is described by Eq. (6), but we have also to consider the *transport* of *slow* electrons from their point of production to the surface. This can be done by introducing diffusion (attenuation) functions

$$P_B(x)=P\exp\left[\frac{-x}{\lambda_S}\right] \tag{7a}$$

$$P_F(x)=P\exp\left[\frac{-(d-x)}{\lambda_S}\right] \tag{7b}$$

for the beam entrance (B for "backward") and the beam exit side (F for "forward"). Here, λ_S is the characteristic diffusion length for low-energy electrons, and P denotes the surface *transmission* probability. $P(E,\theta,U)$ depends on the energy (E) and angle with respect to the surface normal (θ) of electrons approaching the surface and the height of the surface potential barrier (U) and is in the order of 0.1–0.5 [12,13].

Although these diffusion or attenuation functions Eq. (7) closely resemble Eq. (6), the δ-electron transport function, Eq. (6), is by far more complicated in its meaning. Equations (7a) and (7b) describe the diffusion of low-energy electrons with an initially isotropic angular distribution. Equation (6) describes the production at $x>0$ of such low-energy electrons (with isotropic angular distribution) by δ electrons produced at $0<z<x$. The angular distribution of the δ electrons is thus assumed in Eq. (6) to be strongly forward peaked.

Now, we are ready to calculate the *low-energy* electron emission yields, i.e., the number of emitted electrons per incoming projectile. We add up the production terms Eqs. (2) and (4) and multiply by the diffusion functions which include the surface transmission factor Eqs. (7a) and (7b). By integrating over dx from 0 up to the target thickness d, we obtain the target-thickness-dependent forward (F) and backward (B) yields of low-energy electrons,

$$\gamma_{F/B}(d)=\int_0^d[dN_{\mathrm{LE}}^{\mathrm{spi}}/dx+dN_{\mathrm{LE}}^{\delta}/dx]P_{F/B}(x)dx\ . \tag{8}$$

It is important to note that the number of high-energy electrons is *not* included in the yields γ directly, but only indirectly by producing low-energy secondary electrons.

By assuming that $\lambda_{\delta}\gg\lambda_S$, and keeping in mind that dE/dx is assumed to be constant for all thicknesses d, the integration results in simple equations for the target thickness dependence of forward (γ_F) and backward (γ_B) electron yields

$$\gamma_B(d)=\Lambda\beta_S(dE/dx)[1-\exp(-d/\lambda_S)]\ , \tag{9}$$

$$\gamma_F(d)=\Lambda(dE/dx)[1-\beta_S\exp(-d/\lambda_S)-\beta_{\delta}\exp(-d/\lambda_{\delta})] \tag{10}$$

with

$$\Lambda=P\lambda_S/\langle W\rangle\ . \tag{11}$$

The "thick target" or, better, "equilibrium" yields are given by the limit $d\to\infty$ of Eqs. (9) and (10):

$$\gamma_B(\infty)=\Lambda\beta_S\,dE/dx\ , \tag{12}$$

$$\gamma_F(\infty)=\Lambda\,dE/dx\ . \tag{13}$$

They represent the yields for foils thicker than the range of high-energy electrons ($d\gg\lambda_{\delta}$) and sufficiently thick to ensure charge equilibration of the ions. Equations (12) and (13) are well established in the case of *proton* impact: Over a wide range of proton energies (from a few keV up to >10 MeV regime), electron yields are proportional to the electron energy loss dE/dx [3,11,16,17]. In this case, the parameter Λ describes the material dependence of electron yields and is thus often called "material parameter."

However, with *heavy ions,* strong deviations from the simple scaling with dE/dx have been observed at low and medium velocities (<1 MeV/u) [3,14], but also at energies as high as 5–6 MeV/u [10,11]. These deviations manifest as electron yield reductions (in one case, also an enhancement has been observed, see Sec. VII) and can be parametrized by introducing the factors C_F and C_B in Eqs. (12) and (13). The "equilibrium yields," $\gamma_B(\infty)$ and $\gamma_F(\infty)$, for *heavy ions* can then be written as

$$\gamma_B(\infty)=\Lambda\beta_S C_B(Z_P,v_P)\,dE(Z_P,v_P)/dx\ , \tag{14}$$

$$\gamma_F(\infty)=\Lambda C_F(Z_P,v_P)\,dE(Z_P,v_P)/dx \tag{15}$$

as discussed in Refs. [14,18]. Thus, in the proton case, $C_{F/B}(Z_P=1,v_P)=1$, and in the heavy ion case, if yield reductions occur, $C_{F/B}(Z_P>1,v_P)<1$. These factors are a measure for the deviation of electron yields from a simple scaling with the electronic energy loss $dE(Z_P,v_P)/dx$ of the projectiles,

$$C_{F,B}(Z_P,v_P)=[\gamma_{F,B}(Z_p)/\gamma_{F,B}(\mathrm{H}^+)] \times\left[\frac{dE}{dx}(\mathrm{H}^+)/\frac{dE}{dx}(Z_p)\right] \tag{16}$$

under the assumption that $\beta_S(Z_p)=\beta_S(\mathrm{H}^+)$ for C_B.

The results (concerning *backward* yields) have been interpreted in terms of the following two different models:

(1) Rothard, Schou, and Groeneveld [14] proposed that electron yield reductions for ions of about 0.1–2 MeV/u could be due to *variations in stopping power* near the surface, which result from *pre-equilibrium variations of the effective ion charge* $q^*(x)$ as a function of the penetration depth, if most of the emitted electrons originate from within a depth much smaller than the depth needed to reach charge equilibrium. We will come back to this in connection with the observed incident charge state (q) dependence in Sec. V. For more details, we refer the reader to Ref. [14].

(2) On the other hand, a model in terms of *electron trapping in the wake of the ions due to an attractive track potential* ϕ_{TR} has been proposed by Borovsky and Suszcynsky [11]. Consider a completely stripped ion of high enough velocity to ensure charge state conservation over a penetration distance much larger than the electron escape depth. Such an ion creates, due to the high density of ionization, a positively charged track in its wake. As a result, the attractive track potential ϕ_{TR} causes an attractive force which retains a certain number of the electrons liberated and moving away from the ion track. Consequently, electron yields will be reduced.

The main predictions of the attractive track potential model are (1) The yield reduction increases with increasing Z_P or q for $v_P=$const (because of the increasing ionization density). (2) The effect decreases with v_P and disappears in the high-velocity limit $E_P>100$ MeV/u. Within this "trapping in the wake" model, the (backward) "reduction factors" can be written as [19]

$$C_B(Z_P,v_P)=[(I+e\phi_{\mathrm{TR}})^{-1}-E_{BE}^{-1}]/(I^{-1}-E_{BE}^{-1}) \tag{17}$$

with the maximum momentum transfer in a binary encounter collisions corresponding to an electron energy of $E_{BE}=2m_e v_P^2$, the mean ionization potential I and the track potential ϕ_{TR}.

It is interesting to note that the ion track potential ϕ_{TR} can be calculated from Eq. (17) if I is known. We have to keep in mind that I is only an empirical parameter adjusted to fit experimental data. Also, Eq. (17) is only valid for highly charged or completely stripped ions with an effective charge close to Z_P. If this is not the case, i.e., if we consider lower velocities or ions that still carry many electrons, an effective charge has to be introduced in Eq. (17) as discussed in Ref. [14]. It is not clear to us whether a similar expression as Eq. (17) can be given in a straightforward way for the forward yields, since the forward-peaked high-energy electrons might be of major importance. The calculations of Ref. [11] have been made for backward emission only.

III. NUMERICAL SIMULATION OF ELECTRON TRANSPORT

As can be seen from Eqs. (9) and (10) and Fig. 1, the analysis of measurements of the target thickness dependence of forward- and backward-electron yields—within the framework of the semiempirical model of EE—allows one to calculate the characteristic transport length λ_δ in the direction *parallel* to the ion trajectory. In order to also obtain information about the *perpendicular* component $\lambda_\perp^{\mathrm{MC}}$ of the electron transport length, we have performed a MC simulation of electron production and transport in solids based on the work of Gervais and Bouffard [20]. Also, the value of the calculated longitudinal component $\lambda_\delta^{\mathrm{MC}}$ can be compared to values of λ_δ obtained from target-thickness-dependent electron yield measurements. The procedure of deduction of $\lambda_\perp^{\mathrm{MC}}$ and $\lambda_\delta^{\mathrm{MC}}$ from the numerical simulations and the results are discussed in Sec. VI.

The projectiles are treated as point charges of constant kinetic energy with a straight trajectory and an effective charge $q^*(Z_P,v_P)$, i.e., electron capture and loss as well as projectile excitation are not taken into account explicitly. The target material, carbon, is treated as homogeneous and isotropic and is characterized by its atomic number and mass ($Z_T=6$, $A=12$), density ($\rho=1.65$ g/cm^3), Fermi energy $E_F=17$ eV and corresponding plasmon excitation frequency ($\hbar\omega_P=21.2$ eV), and finally the $1s$ ionization energy $U_{1s}=284$ eV. The density of electronic states is divided in two parts: atomic core levels and free valence electron gas. The band structure is not taken into account explicitly.

Primary ionization of core levels is calculated in first Born approximation using hydrogenic wave functions [21]. Valence electrons are treated in the framework of the dielectric theory [22]. In particular, plasmon excitation and subsequent creation of secondary electrons due to plasmon decay in electron-hole pairs is taken into account. The lifetime of the plasmons was deduced from optical measurements [23] neglecting the wave-number (k) dependence.

Secondary ionization processes induced by electrons with enough energy to generate cascade electrons are treated in the same way as primary ionization by the ions. The electrons and all secondaries from cascade multiplication released by primary ionization are transported through the solid on classical trajectories. In view of the de Broglie wavelength, this is a good assumption for the high-energy electrons ($E\gg100$ eV) of interest here. All electrons are followed until they reach a kinetic energy of less than a cutoff value of $E_{\mathrm{co}}=2$ eV. This value has been chosen because it can be expected that such low-energy

electrons do not further ionize and remain confined within a small volume with respect to the diffusion lengths $\lambda_\perp$ and λ_δ of high-energy electrons (Fig. 1). The energy levels are counted with respect to the Fermi level E_F. Approximately 5×10^4 electrons from primary ionization events were followed in order to obtain good statistics. The calculation is described in detail in Ref. [20].

As we are interested in characteristic transport lengths of electrons in directions perpendicular and parallel to the ion track, we use the MC simulations to calculate internal radial and longitudinal electron distributions dN/dr and dN/dx, respectively. From the numerical simulations, the density of electrons $d^3n(x,y,z)/(dx\,dy\,dz)$ of a kinetic energy of less than a cutoff value of E_{co} at (x,y,z) can be obtained. By integrating over x, (i.e., projecting the electron positions on a plane perpendicular to the ion track, we obtain radial distributions $dN(r)/dr$ of the density of electrons as a function of the distance r from the ion track. In order to allow a direct comparison of these plots (Fig. 2) to the widely used plots of deposited energy in track structure calculations [20], the azimuth angle integration has not been performed. By integrating over the cylindrical coordinates r and ϕ (which correspond to the symmetry of the problem), we obtain longitudinal distributions $dN(x)/dx$ of electrons emitted into a layer between x and $x+dx$ if primary ionization occurred at $x=0$. Both distributions are connected by

$$\int_0^\infty r\,dr\int_0^{2\pi}d\phi\,dN(r)/dr=N_{\text{intern}}=\int_{-\infty}^{\infty}dx\,dN(x)/dx\ . \qquad (18)$$

The constant values N_{intern} of the integrals in Eq. (18) represent the total number of internally produced low-energy electrons in a layer of thickness dx.

Figure 2 shows the radial distribution $dN(r)/dr$ as a function of the radial distance r from the ion track for C, S, and Ar projectiles with incident energies of 1, 3.9, and 13.6 MeV/u, respectively. Two different cases have been investigated (1) electron creation by all electrons (primary, secondary, tertiary, . . .) of all energies $E>E_{co}=2$ eV (upper curves) and (2) electron creation by primary high-energy δ electrons $E>100$ eV only (lower curves). Above a certain distance R_0 from the ion track, the two curves are seen to merge. For $R<R_0$, much more low-energy electrons are created if electron creation by all electrons is taken into account. But for $R>R_0$, low-energy electrons are mainly created by high-energy primary electrons. In the case of Ar ions, electrons with energies below 100 eV deposit their energy within a radius of about $R_0\approx60$ Å.

Also shown are the distributions $dN(x)/x$ as a function of the distance x from the point of primary ionization in Fig. 3. The primary ionization events take place at $x=0$ within the (infinite) carbon target. We thus obtain the distributions in the direction of the ion trajectory (forward emission, right-hand side of Fig. 3), and in the inverse direction (backward emission, left-hand side of Fig. 3) for the same projectiles as in Fig. 2. From Figs. 2 and 3, we see that more electrons are created at small radial or longitudinal distances with S than with Ar and C. This is in agreement with the experimental results: the to-

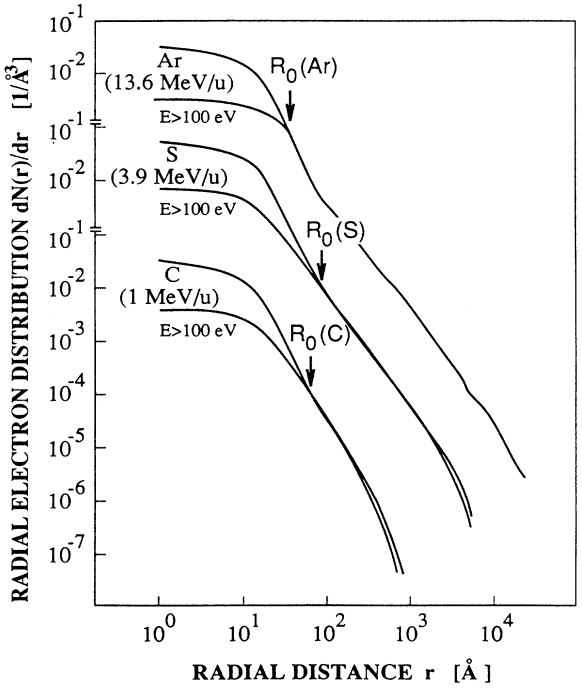

FIG. 2. Radial electron distributions dN/dr (see text, projectiles and energies as indicated) from numerical (MC) simulations as a function of the radial distance r from the ion track. Two different cases are shown: electron creation by electrons of all energies ($E>2$ eV, upper curves) and electron creation by primary high-energy δ electrons only ($E>100$ eV, lower curves). Both curves fall together at $R_0(Z_p,v_p)$.

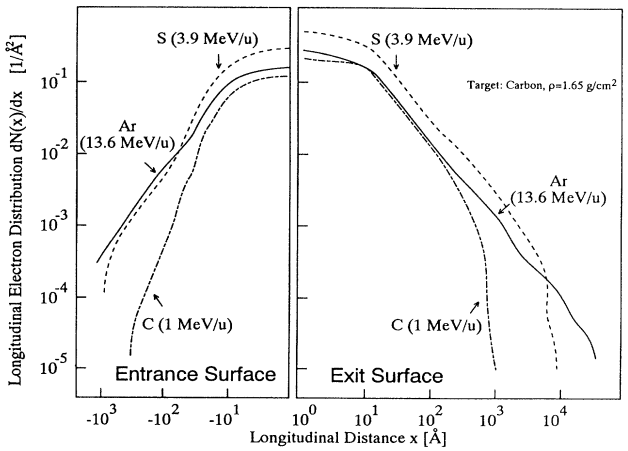

FIG. 3. Longitudinal distributions $dN(x)/x$ (from the MC simulations) as a function of the distance x from the point of primary ionization in the direction of the ion trajectory (forward emission, right-hand side) and in the inverse direction (backward emission, left-hand side). Ions as indicated (same as in Fig. 2).

tal yields are $\gamma_T \approx 120$ for S, $\gamma_T \approx 70$ for Ar, and $\gamma_T \approx 45$ for C. From both figures it can clearly be seen that the Ar-induced electron distribution extends over much larger distances. Ar induces electrons of much higher energy and range, since the maximum velocity of δ electrons depends linearly on the projectile velocity (about 4:2:1 for Ar, S, and C, respectively).

The present MC code can also be used to calculate forward and backward electron yields. Primary ionization occurs at a position x' chosen arbitrarily in a target of thickness d. All electrons liberated by primary or secondary ionization events are followed from their point of liberation x' inside the target, $0 \le x' \le d$, until they reach either $x=0$ (backward surface) or $x=d$ (forward surface). Then, if their kinetic energy is higher than the work function of $\phi \approx 5$ eV, they are considered as being ejected into the vacuum and counted for the calculation of the mean electron yields γ_F^{MC} and γ_B^{MC}. Results are shown and discussed in Sec. V.

IV. EXPERIMENTAL SETUP

The experimental setup as shown in Fig. 4 is similar to the one of Ref. [24] and has been described in more detail previously [18,25]. The experiments were performed at the "Grand Accelérateur National d'Ions Lourds" (GANIL) in Caen/France. The Ar^{q+} beams (13.6 MeV/u, $q=16-18$) were focused so that the beam spot size on the target was less than 4 mm. Typical beam currents were in the order of 1–10 particle nA. The experiments were performed in standard high vacuum ($p \approx 10^{-4}$ Pa). We observed that electron yields decreased with time of exposure to the heavy ion beam (i.e., with the ion fluence) until a nearly constant value was reached after typically 10–20 min. Similar observations have been made in ultrahigh vacuum [3,26], but also before under standard vacuum conditions (see, e.g., [27]). This is probably caused by evaporation of surface contamination such as water and hydrocarbon molecules: After a certain ion fluence, an equilibrium between desorption and reabsorption from the residual gas is reached. Also, modification of the surface structure has to be considered [3,26].

Total yields γ_T can easily be obtained by measuring the ion-induced target current I_T and the ion-beam current I_{FC} with a Faraday cup equipped with a repeller ($U_{REP}=-300$ V) taking into account the mean final charge q_f and the incoming charge state q of the ions [24]. The forward and backward electron yields (γ_B and γ_F) have been obtained by directly measuring the current of low-energy electrons, I_B and I_F, with two cylindrical Faraday cups on the beam entrance (B) and exit (F) side of the thin carbon foils as described in Refs. [18,25]. The cups are held at a potential of +45 V, the target holder and grids in front of the cups at −45 V in order to assure complete collection of all low-energy electrons ($E \ll 100$ eV). However, electrons with energies exceeding about 100 eV which are emitted in extreme forward (0°–15°) or backward (165°–180°) direction can escape from the cups. Thus, the quantity

$$\gamma_\delta = \gamma_T - \gamma_{SE} \tag{19}$$

with

$$\gamma_{SE} = \gamma_B + \gamma_F \tag{20}$$

gives a qualitative information about high-energy (δ) electrons ($E > 100$ eV), whereas γ_{SE} is a measure of low-energy (SE) electron emission. Error bars for low-energy electron yields are in the order of ±6–8 % [18,24,25].

The thin self-supporting target foils have been produced by standard evaporation techniques at the "Institut de Physique Nucléaire" in Lyon/France. A surface barrier detector mounted under an observation angle of 14° with respect to the exit beam direction was used to measure elastically scattered primary Ar ions and C recoil ions in order to determine the relative thickness of the carbon foils with an accuracy of about ±10%. It was observed that the thickness (or, more precisely, the number of scattering target atoms in a given beam diameter) decreased with the ion fluence. This may either be caused by sputtering or a change of target density. We assume the density of our carbon foils to be $\rho = 1.65$ g/cm^3. This value has been obtained by an interferometric method and Rutherford scattering analysis [28].

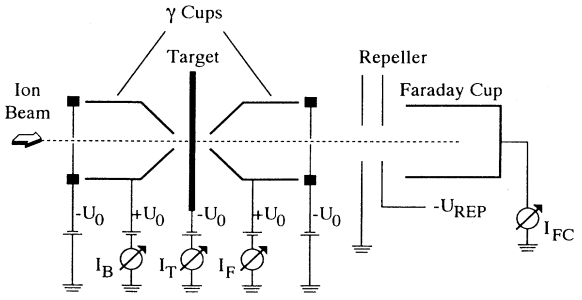

FIG. 4. Experimental setup for forward and backward low-energy electron yield measurements (schematic, for details, see text).

V. ANALYSIS OF TARGET-THICKNESS-DEPENDENT ELECTRON YIELDS WITHIN THE SEMIEMPIRICAL MODEL: PRIMARY IONIZATION VERSUS CASCADE MULTIPLICATION

The dependence of total (T), forward (F), and backward (B) electron yields on target thickness are shown in Figs. 5–7 for Ar^{q+} ions of incoming charge states $q=16$ (Fig. 5), $q=17$ (Fig. 6), and $q=18$ (Fig. 7). For comparison, γ_T data obtained with Ni^{26+} (15.2 MeV/u) at UNILAC in Darmstadt [29] have been included in Fig. 5 (labeled Ni). Both projectiles, Ar^{16+} and Ni^{26+}, carry two electrons in the closed K shell. Also shown are the low-energy electron yields, $\gamma_{SE}=\gamma_B+\gamma_F$, together with the results of least-square fits of the sum of Eqs. (9) and (10) to the experimental data. Furthermore, the high-energy δ-electron yields $\gamma_\delta=\gamma_T-\gamma_{SE}$ are included.

We state that forward yields γ_F are always higher than backward yields γ_B, for all target thicknesses and all

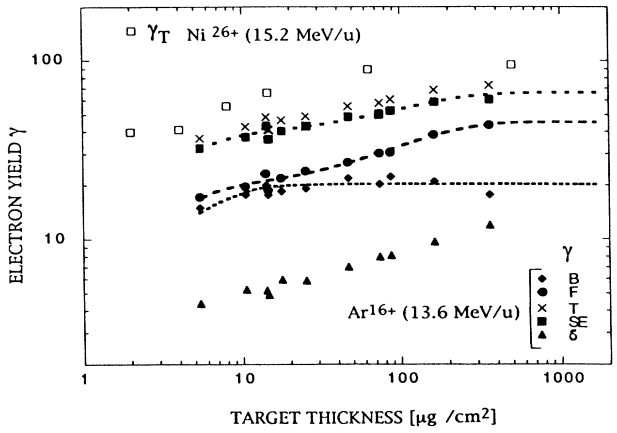

FIG. 5. Total (T), forward (F), and backward electron (B) yields as a function of target thickness (carbon foils) obtained with fast heavy ions (Ar^{16+}, $v_P=23$ a.u., $E_P=13.6$ MeV/u) at GANIL in Caen. Also included are $\gamma_\delta=\gamma_T-\gamma_{SE}$ (labeled δ) and $\gamma_{SE}=\gamma_B+\gamma_F$ (labeled SE), see text, as well as γ_T data obtained with Ni^{26+} (15.2 MeV/u) [29] (labeled Ni). Also shown are the results of least-squares fits of Eqs. (9) and (10) to the experimental values and to the low-energy electron yields, $\gamma_{SE}=\gamma_B+\gamma_F$.

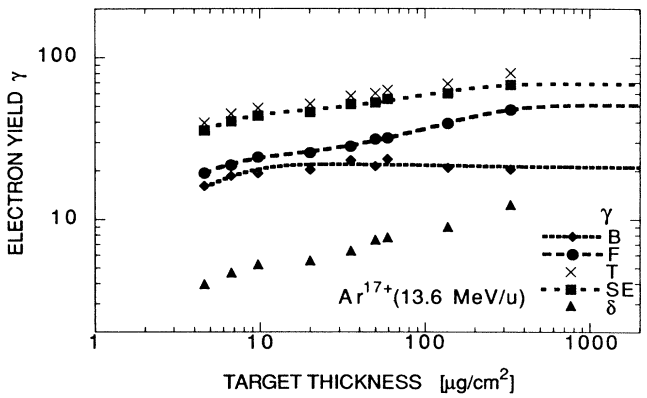

FIG. 6. Same as Fig. 4, but for Ar^{17+} projectiles.

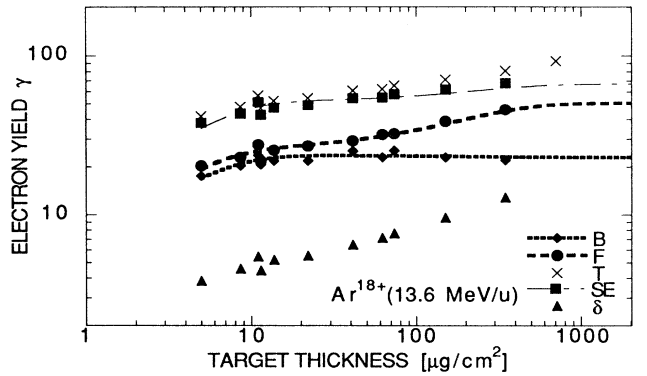

FIG. 7. Same as Fig. 4, but for Ar^{18+} projectiles.

charge states. However, it is obvious that γ_F and γ_B show a quite different dependence on target thickness. This becomes more evident in Figs. 8 and 9, which present γ_B and γ_F for the three charge states ($q=16,17,18$) as a function of target thickness d (note the linear scale for the electron yields). Also shown are fits of Eq. (9) to γ_B in Fig. 8 and Eq. (10) to γ_F in Fig. 9. The backward yields increase with d, but—in comparison to the forward yields—rapidly reach a saturation value $\gamma_B(\infty)$ (which, however, depends on q).

In contrast to the thickness dependence of the backward yields $\gamma_B(d)$, the forward yields $\gamma_F(d)$ do not cease to increase within the target-thickness range studied (4–360 $\mu g/cm^2$). The fitted curves from the semiempirical model shown in Figs. 5–7 and in Fig. 9 suggest that a saturation of γ_F is reached at about 400–500 $\mu g/cm^2$. This conclusion is supported by the total-yield data shown in Fig. 7 for Ar^{18+} (5–700 $\mu g/cm^2$, compare the shape of the curves shown for γ_F and γ_{SE} to the increasing total yield), and also by the total yield data for Ni^{26+} of Fig. 5 (2–500 $\mu g/cm^2$, at comparable velocity). It should clearly be noted that only the combination of data points and shape of the fit suggest the conclusion that the forward yields saturate at about 400–500 $\mu g/cm^2$. It can, however, be expected that such a saturation must occur. While the backward yields clearly depend on the charge state of the incoming ions, i.e., $\gamma_B(q=18)>\gamma_B(q=17)>\gamma_B(q=16)$ (Fig. 8), no such dependence can be stated for the forward yields γ_F (Fig. 9) within the estimated errors of ±6–8 %.

The high-energy δ electron yields are shown in Fig. 10. Their dependence on d is similar to that of γ_F: a strong increase with d. Taking into account the saturation of the total yields, we can assume that a saturation of γ_δ may be reached beyond ≈400 $\mu g/cm^2$. These δ electrons represent a fraction of ≈9–18 % of the total electron yields. A striking result is that clearly no dependence on the charge state q can be seen. This can be explained easily, since these electrons result from close collisions where screening by the projectile electrons does not play an important role.

In order to discuss the dependence of the electron yields on the target thickness (Figs. 5–10) in more detail, we show in Fig. 11 the ratios of forward and backward yields, obtained with incoming charge states $q=16$ and $q=17$, to yields obtained with $q=18$. We denote these ratios $R_{F,B}(d)=\gamma_{F,B}(q)/\gamma_{F,B}$ (18). These quantities allow one to study the influence of the projectile electrons on electron yields in an easy way: if the charge state of the incoming ions does not affect electron emission, a value of $R_{F,B}=1$ is expected. Additional electron emission due to the incoming electrons would lead to $R_{F,B}>1$ (as it has been observed with MeV/u molecular hydrogen ions [24]), electron yield reductions (e.g., due to screening of the projectile charge) lead to $R_{F,B}<1$. Also included in Fig. 11 are the backward and forward yields obtained with Ar^{18+}. The mean charge $\langle q\rangle=17.85$ of Ar at 13.6 MeV is close to $Z_P=18$.

The following discussion elucidates an important result of the present studies: By comparing bare and electron-carrying high-velocity heavy ions, it becomes possible to

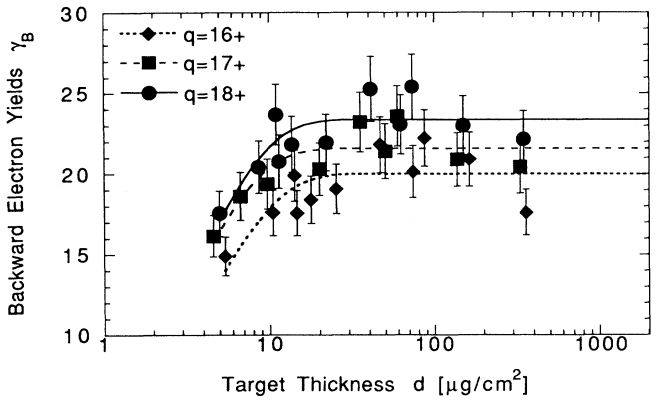

FIG. 8. Backward yields γ_B for Ar at 13.6 MeV/u for the three charge states ($q=16,17,18$) as a function of target thickness d on a linear scale for the electron yields. Also shown are fits of Eq. (9) to γ_B.

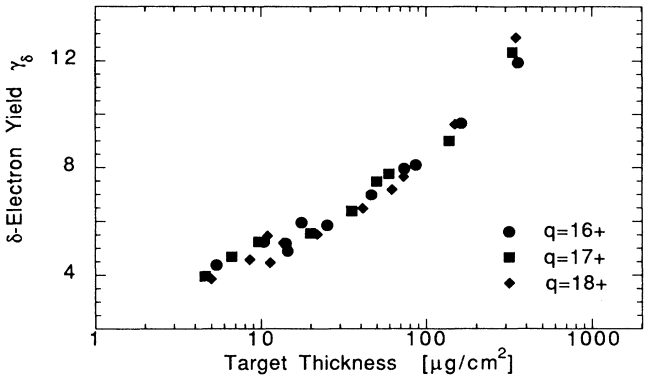

FIG. 10. δ-electron yields γ_δ for Ar at 13.6 MeV/u for the three charge states ($q=16,17,18$) as a function of target thickness d on a linear scale for the electron yields.

distinguish secondary electron production by high-energy δ electrons (cascade multiplication, CM) from electron production by primary ionization (PI), since electron production is roughly proportional to dE/dx and thus to the square of the effective charge $q^*(x)$ [14]. The dependence of the effective charge on the penetration depth x (which is due to electron capture and loss) determines the electron production by PI.

From Figs. 8 and 11, we can draw the following conclusions on the backward yield (and R_B) dependence on target thickness:

Region (I). For $d<15$–20 μg/cm², one observes an increase of both γ_B and R_B with d until constant values are reached. This behavior depends on increasing electron production with increasing target thickness, and possibly, the evolution of the secondary electron cascade multiplication caused by backscattered δ electrons (see next section).

Regions (II–IV). For $d>15$–20 μg/cm², the ratios R_B are constant and equal to $R_B(\infty)=\gamma_B(\infty,q)/\gamma_B(\infty,18)$.

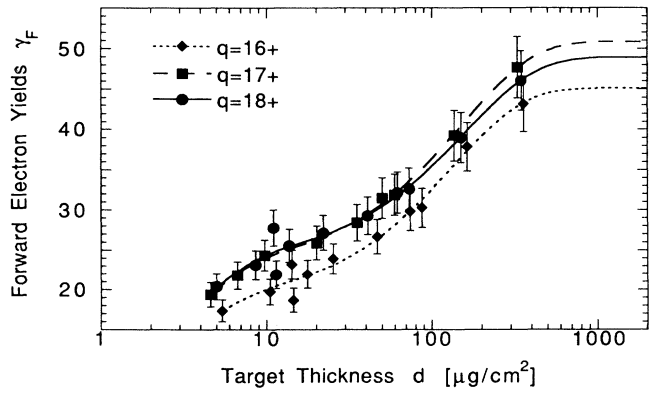

FIG. 9. Forward yields γ_F for Ar at 13.6 MeV/u for the three charge states ($q=16,17,18$) as a function of target thickness d on a linear scale for the electron yields. Also shown are fits of Eq. (10) to γ_F.

The incoming charge state (q) dependence is due to the fact that for fast projectiles the initial charge state is conserved over distances λ_q much larger than the characteristic low-energy electron transport lengths $\lambda_s \ll \lambda_q$. In the present case, about 50% of incoming Ar^{17+} or Ar^{16+} ions have changed their charge state to $q_i=18$ after ≈ 120 μg/cm² (to be compared to $\lambda_S \approx 3$ μg/cm²,

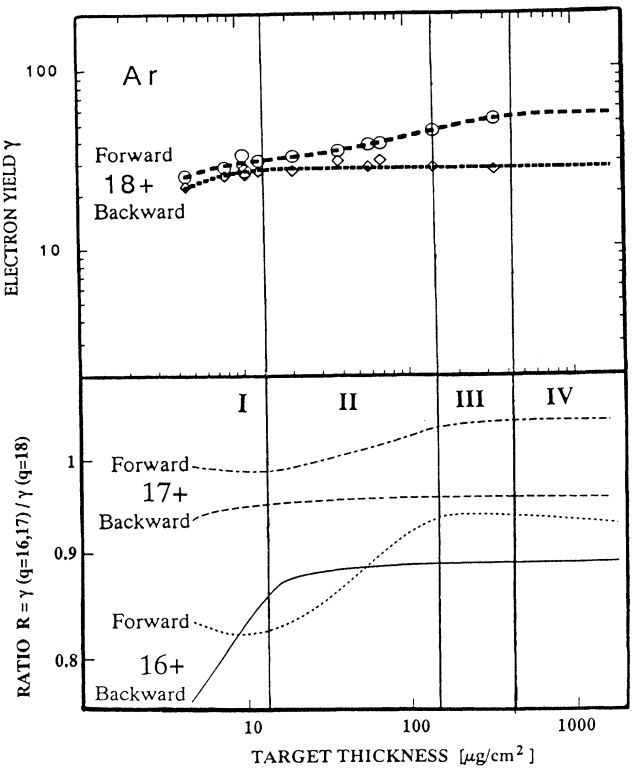

FIG. 11. Ratios of forward (and backward) yields obtained with incoming charge state $q=16$ and $q=17$ to yields obtained with $q=18$, i.e., $R_{F,B}(d)=\gamma_{F,B}(q)/\gamma_{F,B}$ (18). Also included are the backward and forward yields obtained with Ar^{18+} (top). Experimental errors are estimated to be ±(6–8)% for yields and about ±12% for the ratios R.

see Table I). Thus, as the yields scale approximately as $\gamma \sim [q(d \approx \lambda_S)]^2$ [12,14], we find $R_B(\infty)=0.92$ (0.84) for $q_i=17$ (16), versus $[\langle q \rangle(q_i)/\langle q \rangle(18)]^2=0.91$ (0.81).

From Figs. 9 and 11, we can distinguish four regions (labeled I, II, III, and IV) characterizing the forward yield γ_F (and R_F) evolution with increasing target thickness:

Region (I). Below $\approx 10-15$ $\mu g/cm^2$, we are close to single collision conditions and the incoming charge state is conserved for most of the projectiles. Thus, the projectile charge is screened by the electron(s) leading to lower yields for $q=16$ and $q=17$ (compare the above discussion of the incoming charge state dependence of the backward yields). The yields γ_F always increase, because the number of liberated electrons from PI increases with target thickness. The target is so thin that CM is just beginning to start: most δ electrons leave the foil without dissipating their energy in the target.

Region (II). Between ≈ 15 and 150 $\mu g/cm^2$, the yields γ_F and R_F increase strongly. Both charge changing (R_F, leading to increasing PI electron production cross sections with increasing charge state) and CM account for this.

Region (III). Between 150 and 400 $\mu g/cm^2$, R_F values are constant and approximately equal to 1, but the yields still increase. The incoming charge state is "forgotten," the mean charge nearly 18, and PI electron production per unit path length is constant. The additional fraction of low-energy electrons leading to increasing yields must be due to the evolution of the low-energy electron CM induced by fast electrons from deeper layers.

Region (IV). At $d > 400-500$ $\mu g/cm^2$, γ_F and R_F have reached constant values: both charge equilibrium ($d_{eq} \approx 450$ $\mu g/cm^2$) and full development of the secondary electron cascade induced by high-energy δ electrons [$\gamma_\delta(\infty)$ for $d > 400-500$ $\mu g/cm^2$] are reached.

Finally, let us note that $R_F(d=\infty)$ should not depend on the initial charge state. Thus, the deviation from unity, $R_F(\infty, q=17) \approx 1.04$ and $R_F(\infty, q=16) \approx 0.92$ is compatible with and a measure for the experimental error of ±6–8 % for the yields. However, for analysis within the semiempirical model, it is rather the shape of the yield curve than its absolute value which is important.

TABLE I. Electron transport lengths from analysis of the experimental data (λ_S diffusion length of low-energy electrons, λ_δ transport length of fast electrons) and from the numerical (MC) simulations (for fast electrons: $\lambda_\perp^{MC}$ radial, λ_δ^{MC} longitudinal forward, $\lambda_\delta'^{MC}$ longitudinal backward). Also, the partition factor β_δ [see Sec. II, Eq. (1) for definition] is included.

Z_P	$_{10}$Ne	$_{6}$C	$_{16}$S	$_{18}$Ar
E_P/M_P (MeV/u)	0.1	1.0	3.9	13.6
β_δ	0.42±0.03	0.54±0.05	0.59±0.05	0.55±0.02
λ_S (Å)		17±3	14±2	180±15
λ_δ (Å)	≪200	300±26	1200±50	9000±680
λ_δ^{MC} (Å)		70	450	2600
$\lambda_\delta'^{MC}$ (Å)		3	15	56
$\lambda_\perp^{MC}$ (Å)		80	570	4000

To complete the results on the target thickness dependence, in Fig. 12 we show forward- and backward-electron yields as calculated with the MC simulation (labeled MC) described in Sec. III. Also shown is their sum, the total electron yield $\gamma_T^{MC}=\gamma_F^{MC}+\gamma_B^{MC}$ as a function of carbon target thickness. The collision system is Ar^{17+} ions at 13.6 MeV/u on carbon foils. Also included are experimental results for the total yields γ_T and the backward and forward yields γ_B and γ_F.

When comparing the experimental forward and backward "low-energy electron yields" to the calculated ones, one has to keep in mind that the simulated yields also contain the high-energy electrons of $E > 100$ eV, which are not collected by our experimental setup. It would, however, in principal be possible to introduce an upper cutoff energy as a boundary in order to calculate "low-energy electron" forward and backward yields. Since it would be somewhat arbitrary to introduce such a boundary $\langle E \rangle$ (see above), we prefer to show the yields calculated without such a boundary and including all electrons. When comparing them to the experimental forward and backward yields, one has to keep in mind that they may be up to about 15% higher due to contributions of the fast electrons. The difference can be expected to be less important for the backward yields than for the forward yields, since most of the fast electrons are emitted in forward direction.

The experimental data for total yields $\gamma_T(d) = \gamma_B+\gamma_F+\gamma_\delta$ agree within 30% with the calculated yields $\gamma_T^{MC}(d)=\gamma_F^{MC}+\gamma_B^{MC}$. Also, the evolution of the yields with target thickness is reasonably well reproduced: simulated backward yields are found to be independent of the target thickness, forward yields increase strongly. In view of the fact that specific heavy ion related effects, as for example, the trapping of electrons in the ions wake (as described in Sec. II), are not included in the simulations, this is a promising result. The specific properties of heavy ions are only taken into account by introducing an effective charge.

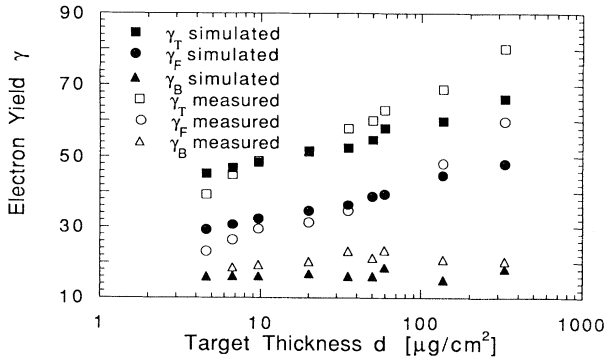

FIG. 12. Calculated (from the numerical MC simulations) forward and backward electron yields and their sum, the total electron yield $\gamma_T^{MC}=\gamma_F^{MC}+\gamma_B^{MC}$ as a function of carbon target thickness for Ar^{17+} at 13.6 MeV/u. Also included are experimental results for the total yields γ_T.

VI. ELECTRON TRANSPORT LENGTHS FROM THE SEMIEMPIRICAL MODEL AND NUMERICAL SIMULATIONS

As discussed in Sec. II, the measurement of the target-thickness dependence of electron yields allows the application of the semiempirical model Eqs. (9) and (10). The diffusion length for low-energy electrons λ_S and the *longitudinal* transport length for high-energy electrons λ_δ as obtained from curves fitted to our *experimental* Ar data (shown in Figs. 5–9), are summarized in the last column of Table I.

In order to obtain a first approach for a "characteristic transport length" $\lambda_\perp$ in the direction *perpendicular* to the ion trajectory, the most reasonable procedure seems to utilize the first moment of the calculated distribution $dN(r)/dr$ (Fig. 2)

$$\lambda_\perp^{\mathrm{MC}}=\frac{\int_0^\infty [dN(r)/dr]r\,dr}{\int_0^\infty [dN(r)/dr]dr} . \tag{21}$$

Longitudinal transport lengths can be obtained in complete analogy to the procedure described above from the first moments of the longitudinal distributions dN/dx shown in Fig. 3. From the right-hand side of Fig. 3, we obtain transport lengths in forward direction ($\lambda_\delta^{\mathrm{MC}}$) and from the left-hand side of Fig. 3 transport lengths for backscattered δ electrons in backward direction ($\lambda_\delta'^{\mathrm{MC}}$).

In order to study the velocity dependence of all the quantities characterizing electron transport in solids from heavy ion induced electron emission yields, we have included previous work with Ne (0.1 MeV/u) [18], C (1 MeV/u), and S (3.9 MeV/u) ions [12] in Table I. Shown are λ_S, λ_δ, $\lambda_\perp^{\mathrm{MC}}$ (radial), $\lambda_\delta^{\mathrm{MC}}$ (longitudinal, forward), $\lambda_\delta'^{\mathrm{MC}}$ (longitudinal, backward) obtained for carbon targets.

From Eqs. (9) and (10) we can additionally extract the partition factor β_δ, which we also included in Table I. We find from our measurements, in good agreement with the equipartition ($\beta_\delta \approx 0.5$) expected for high-velocity ions [13] β_δ (Ar at 13.6 MeV/u) = 0.55±0.02. This means that although high-energy electrons represent only about 15% of the total electron yield, slightly more than 50% of the projectile kinetic energy lost by ionization is transferred to them. Similar values of β_δ have been found for fast projectiles, i.e., β_δ(S at 3.9 MeV/u) = 0.59±0.05 and β_δ(C at 1 MeV/u) = 0.54±0.05. At lower velocities, but above the threshold velocity for plasmon excitation, the role played by collective excitation processes related to soft collisions with large impact parameter ($\beta_s = 1-\beta_\delta$) becomes more and more important, and consequently β_δ is smaller (=0.42) for Ne at 0.1 MeV/u. Also, the mean energy of the electrons decreases with decreasing projectile velocity, and thus the secondary electron cascade becomes less important.

Coming back to the discussion of the characteristic transport lengths obtained from the analysis of the target-thickness dependence of electron yields within the semiempirical model, we state that their values are found to be much larger in the case of Ar (13.6 MeV/u). The diffusion length of low-energy electrons is found to be $\lambda_S = (180\pm20)$ Å ≈ 3 μg/cm^2 (to be compared with $\lambda_S \approx 15$ Å for S and C) and the transport length of fast electrons is $\lambda_\delta = (9000\pm680)$ Å ≈ 150 μg/cm^2. Taking into account that $\lambda_\delta = 300$ Å for C at 1 MeV/u and $\lambda_\delta = 1200$ Å for S at 3.9 MeV/u, we observe a strong increase of λ_δ with increasing projectile velocity. This is reasonable, as the maximum momentum transfer and the mean electron energy and, consequently, the range of the fast electrons increase with projectile velocity $v_P(\mathrm{Ar}) \approx 2v_P(\mathrm{S}) \approx 4v_P$ (C). The same behavior is found for the velocity dependence of the radial lengths $\lambda_\perp^{\mathrm{MC}}$.

From the numerical simulations (MC), we obtain values $\lambda_\delta^{\mathrm{MC}}$ which are about three times smaller than λ_δ, but which show the same dependence on the projectile velocity. This is a confirmation that both quantities, λ_δ and $\lambda_\delta^{\mathrm{MC}}$, give us an idea of the range and transport length of δ electrons. However, they cannot be compared directly in a quantitative manner. Remember that according to the definition of λ_δ within the semiempirical model, at $x = \lambda_\delta$, about 67% of δ electrons have deposited their energy in low-energy SE cascades, and that $\lambda_\delta^{\mathrm{MC}}$ corresponds to the first moment of the calculated longitudinal electron distribution.

The values for the radial lengths $\lambda_\perp^{\mathrm{MC}}$ give an estimate for the radial range of ion induced energy deposition and damage in materials, the so-called *ultratrack*. We see from Table I that the fast Ar ions of 13.6 MeV/u can induce damage over radial distances as large as 400 nm, compared to less than 10 nm at 1 MeV/u. It would be interesting to study the v_P dependence of the quantities summarized in Table I for a given heavy ion (fixed Z_P) in a large velocity range (0.1–100 MeV/u).

The large value of $\lambda_S = 180$ Å found with Ar (13.6 MeV/u) is surprising, since the isotropic diffusion of low-energy electrons should mainly depend on the target material and not on the projectile type—or velocity. This is indeed what is found for C and S at lower projectile velocity. Probably, the large λ_S value at 13.6 MeV/u could be explained if diffusion of δ electrons in the backward direction was taken into account. Following again Sternglass [13], this can be done by using a more realistic δ-electron energy dissipation and diffusion function than Eq. (6). We have to introduce a third transport length, λ_δ', for energy dissipation in the *backward* direction (opposite to λ_δ). At high projectile velocity leading to high δ-electron energies, it is possible that a considerable fraction of these electrons undergo a few large-angle scattering events and finally propagate in the backward direction with enough energy left to create secondaries.

The modified diffusion function is given by

$$f(x,\lambda_\delta',\lambda_\delta)=\frac{1}{\left[1+\frac{\lambda_\delta'}{\lambda_\delta}\right]}\left[1-\exp\left[\frac{-x}{\lambda_\delta}\right]+\frac{\lambda_\delta'}{\lambda_\delta}\right] . \tag{22}$$

Unfortunately, when replacing Eq. (6) by Eq. (22), the integration of Eq. (8), which is still feasible [17], results in an expression far less simple and elegant as Eqs. (9) and (10). Possibly, the relatively slow increase of γ_B(Ar) with d (Fig. 8) is due to the fact that the slope of the nonequilibrium backward yields are defined by λ_δ' and not by λ_S.

The results of the numerical simulations for $\lambda_\delta'^{MC}$ strongly support this idea: a much larger value is found for Ar than for C or S.

VII. PROJECTILE DEPENDENCE: RELATION TO dE/dx

As already mentioned in Sec. II, strong deviations from a simple scaling of electron yields with the electronic stopping power ($\gamma \sim dE/dx$) have been observed with heavy ions [11,17,18,30]. With one exception (see Table II), electron yield *reductions* $C_{B,F}(Z_p) < 1$ [Eqs. (14)–(16)] have been reported. It is particularly surprising that strong reductions have even been observed with fast, bare ions ($Z_p = 1-8$) at high velocities (5 MeV/u) with thick gold targets [11]. In this case, the effective charge of the ions is close to their nuclear charge, and electron production should scale as the stopping power does, i.e., with Z_p^2. Borovsky and Suszcynsky recently proposed a theoretical model based on the concept of "electron trapping in the wake" [11] which reproduces the experimental results up to $Z_P = 8$ and $v_P = 5$ MeV/u, as discussed in Sec. II. The main result of this theory is expressed by Eq. (17) and can easily be introduced in the semiempirical model Eq. (14).

In order to compare the available experimental results to these predictions, we compiled data on electron emission up to 15 MeV/u with carbon targets. Included are the factors $C(Z_P, v_P)$ as defined by Eqs. (14)–(16) for total, forward, and backward electron yields (indicated, as usual, by the indices T,F,B). The factors $C(Z_p)$ have the same physical meaning as the quotients

$$\Lambda^*_{T,B,F}(Z_P, v_P) = \gamma_{T,B,F}/(dE/dx) \tag{23}$$

(which we have also included in Table II), but are simply scaled and measured in units of $\Lambda(H^+)$. We mention that stopping power tables should be used with care if electron yields are to be compared to the stopping power by calculating the factors Eqs. (14) and (23). In particular at low projectile velocities, it should be carefully checked whether extrapolated dE/dx values really reproduce real stopping power values. However, this is a minor problem for MeV/u ions [31].

From the data shown in Table II, no strong increase of the reduction effect with Z_P for the different ions at comparable velocities (Ne, S, and U around 3.5 MeV/u) can be observed. At about 15 MeV/u, however, the effect is stronger for Ni than for Ar. For $Z_p = 20$, the model [11] predicts much stronger reduction effects (in an order of magnitude of $C_B \approx 0.1$), and this is clearly in contrast with the experimental values. We note that the calculation of the track potential ϕ_{TR} from Eq. (17) from backward yields for carbon targets results in values of one order of magnitude smaller than values deduced from the figures given in Ref. [11] for gold targets.

The reduction effect is always stronger for backward than for forward emission. Furthermore, it seems that with increasing projectile velocity and increasing projectile charge or atomic number, the reduction effect disappears in forward direction: even an enhancement $C_F > 1$ is observed. This is probably due to the increasing contribution of δ-electron induced secondary cascade multiplication in combination with increasing mean electron energy. For details, see the discussion in Ref. [9] on this subject. This is also the reason why at the end of Sec. II we did not introduce the reduction factors given by the attractive track potential model in a straightforward way in the forward-electron yield formula.

In conclusion, because of the lack of systematic studies on the v_P dependence of the "yield reduction effect" for fixed Z_P in a large velocity range (0.1–100 MeV/u), no final conclusions on the validity of the model [11] can be drawn. It is even possible that a saturation of $C(Z_P)$ may be found as a function of Z_P for given v_P, as it has been observed at lower velocities [14,30]. We would finally like to mention that up to now, the reduction of low-energy electron emission has been explained by a screening of the projectile charge by the projectile electrons and by target electrons in metal [3]. However, a variety of other mechanisms have been discussed in order to explain reduction effects, but it is still unclear to what extent each of them contributes. We mention changes of the surface barrier height caused by a charging up near the ion track [10], an interaction of the ion wake with the surface potential [25] and the reduction of the electron production probability due to a high density of electron-

TABLE II. The factors $C(Z_P, v_P)$ as defined by Eqs. (14)–(16) and the quotients $\Lambda^*(Z_P, v_P)$ as defined by Eq. (23) for total, forward, and backward electron yields (indicated by the indices T,F,B) as well as the track potential ϕ_{TR} as calculated from backward electron yields from Eq. (17).

Z_P	$_1$H	$_{10}$Ne	$_6$C	$_{16}$S	$_{10}$Ne	$_{92}$U	$_{92}$U	$_{18}$Ar	$_{28}$Ni
q	1	1	6	16	10	38	68	18	26
E_P/M_P (MeV/u)	0.02–9.5	0.1	1.0	3.9	5	3.5	8.5	13.6	15.2
Λ_T [μg/(keV cm^2)]	11.95	5.1	8.3	8.8	5.6	13.3	12.6	9.1	5.5
Λ_F [μg/(keV cm^2)]	6.55	3.28	4.52		4.4	9.0	10.0	5.15	
Λ_B [μg/(keV cm^2)]	5.45	1.82	3.14		1.2	4.3	2.5	2.44	
C_T	1	0.43	0.69	0.73	0.47	1.11	1.05	0.76	0.46
C_F	1	0.5	0.69		0.67	1.37	1.65	0.78	
C_B	1	0.33	0.58		0.22	0.79	0.46	0.45	
ϕ_{TR}(V)			51		258	20	87	91	
Reference	[16]	[18]	[12]	[12]	[6,9]	[9]	[9]	[This work]	[29]

hole pairs (which then no longer remain uncorrelated) [10].

VIII. CONCLUSION AND OUTLOOK: DOUBLE DIFFERENTIAL ELECTRON SPECTRA

The measurement of electron yields allows the indirect determination of the characteristic transport lengths of high-energy electrons. For more detailed information, spectroscopy studies are needed. To our knowledge, the only systematic measurements of energy and angular distributions induced by swift heavy ions have been performed by Schiwietz and Schneider and co-workers at VICKSI in Berlin with Ne ions and at the Super HILAC in Berkeley with U ions (3.5 and 8.5 MeV/u) [6–9] with thin carbon foils (5–100 $\mu g/cm^2$). Consequently, we measured the evolution of double differential electron spectra $d^2\gamma(\theta)/dv_e d\Omega$ ($E=1$–40 keV, $\theta=0$–$180°$) with carbon target thickness for Ar^{17+}, Ar^{18+} (13.6 MeV/u). As an example, we show in Fig. 13 the angular dependence of δ-electron spectra for Ar^{17+} penetrating C (4.4 $\mu g/cm^2$) at observation angles $0° \le \theta \le 80°$. Further results will be published elsewhere.

Shown in Fig. 13 is the measured intensity as a function of the electron velocity v_e. These spectra, if integrated over all angles, would correspond to a fraction of about 15% of all emitted electrons (compare γ_δ in Figs. 5–7,10). The spectra, taken with a magnetic spectrometer [29], show three main structures. At the low-energy side, electrons from target ionization can be observed. Their distribution extends towards $v_e=0$ with a maximum at some eV [3]. The sharp peak around v_P belongs to "convoy" electrons in low-lying projectile continuum states from electron loss or capture. It disappears slowly with increasing angle, but it can be observed up to $\theta=20°$.

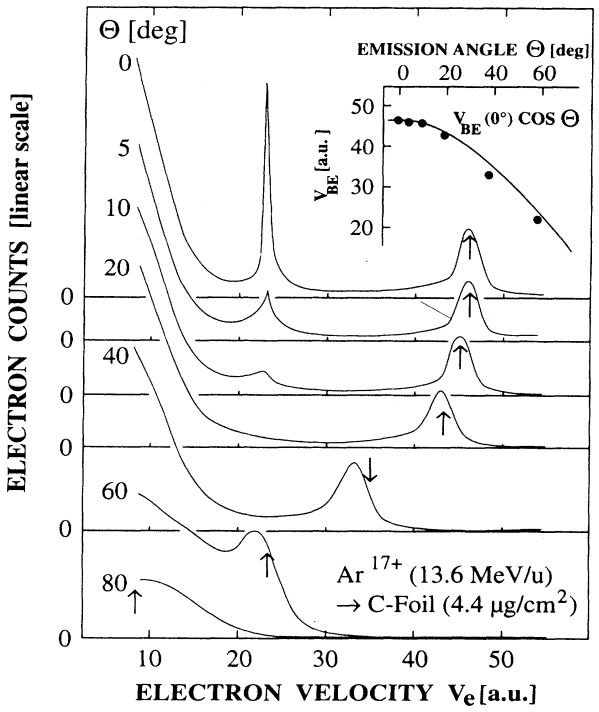

FIG. 13. Doubly differential electron spectra obtained with Ar^{17+} (13.6 MeV/u) at different observation angles $0° \le \theta \le 80°$ from a thin carbon foil ($d=4.4$ $\mu g/cm^2$) as a function of the electron velocity v_e. The expected velocity $v_{BE}=2v_P\cos\theta$ corresponding to the maximum of the binary encounter (BE) electron peak is indicated by arrows and shown as solid line in the inset in comparison to the experimental values obtained from the position of the BE peaks.

The high-energy peak at $2v_P$ stems from "binary encounter collisions." If electron transport phenomena are small, i.e., for sufficiently thin targets, its width represents the initial target electron momentum distribution (COMPTON profile). The angular dependence of the maximum should follow the law $v_{BE}=2v_P\cos\theta$. These theoretical values are indicated by arrows. Surprisingly, we observe slight deviations from this law at large angles $\theta \ge 40°$ as it has been observed in ion-atom collisions at lower energies, too [32].

In conclusion, we have studied electron emission from thin solid foil targets induced by swift heavy ions by means of electron yield measurements, numerical (MC) simulations, and electron spectroscopy. As an important result, due to the high velocity of the heavy ions used in the present studies, it became possible to distinguish secondary electron production by high-energy δ electrons (cascade multiplication) from electron production by primary ionization events.

By combining the experimental results with the numerical simulations, we have obtained electron transport lengths of high-energy δ electrons and also diffusion lengths of slow "secondary" electrons. These transport lengths are a measure for the range of energy deposition by electronic excitation in matter bombarded with heavy ions. Numerical simulations may further enlighten the relation between δ-electron emission and the ion track structure. In this respect, it is necessary to improve the numerical simulations. The first results presented here are promising, and further development of MC simulations thus will provide a useful tool for testing, estimating and predicting experimental outputs [20].

In future experiments, well-defined solid surfaces are necessary and thus, elaborated surface controlling and preparation technology is indispensable. Therefore, we are developing a new experimental ultrahigh vacuum equipment. Further insight in the physics of electron emission and thus ion-solid interaction will be obtained by measurements with heavier particles and by extending studies to higher energy (the 10–100-MeV/u region) for heavy ions with both gaseous and solid targets. Also, the recent development of high-energy beams of heavy ion *clusters* (such as C_n^+ and Au_n^+) leading to increased density of energy deposition at tandem accelerators in Orsay and Erlangen could open a promising new field of investigations [33].

ACKNOWLEDGMENTS

It is a pleasure to thank Daniel Lelièvre and Jean-Marc Ramillon (CIRIL) for their technical assistance before

and during the experiments. Vincent Mouton, Francis Levesque (CIRIL), and Alain Lepoutre (ISMRa, Caen) managed all problems arising with computer software and hardware. We thank GPS/PIIM (Paris, group leader Jean-Pierre Rozet), and in particular Dominique Vernhet, for their friendly help and for lending us their material. Louis Vidal (INPL, Lyon) prepared the high-quality target foils. We thank Jean-Claude Poizat and Joseph Remillieux (INPL, Lyon) for their interest and many helpful discussions. Finally, we thank Gregor Schiwietz (Berlin) for helpful discussions and comments on a preliminary version of the manuscript. One of us (M.J.) acknowledges a grant from CEA and the region of "Basse Normandie."

[1] M. P. Villard, J. Phys. Theor. Appl. **8**, 5 (1899).

[2] J. Devooght, J. C. Dehaes, A. Dubus, M. Cailler, J. P. Ganachaud, M. Rösler, and W. Brauer, in *Particle Induced Electron Emission I,* edited by G. Höhler and E. A. Niekisch, Springer Tracts in Modern Physics Vol. 122 (Springer, Berlin, 1991).

[3] D. Hasselkamp, H. Rothard, K. O. Groeneveld, J. Kemmler, P. Varga, and H. Winter, in *Particle Induced Electron Emission II,* edited by G. Höhler and E. A. Niekisch, Springer Tracts in Modern Physics, Vol. 123 (Springer, Berlin, 1991).

[4] Ionization of Solids By Heavy Particles, Vol. 306 of *NATO Advanced Study Institute, Series B: Physics,* edited by R. Baragiola (Plenum, New York, 1993).

[5] Proceedings of the Second International Symposium on Swift Heavy Ions in Matter SHIM-92, edited by N. Angert, P. Armbruster, and J. C. Jousset [Radiat. Eff. Defects Solids **126**, 1 (1993)].

[6] G. Schiwietz, J. P. Biersack, D. Schneider, N. Stolterfoht, D. Fink, V. J. Montemajor, and B. Skogvall, Phys. Rev. B **41**, 6262 (1990).

[7] G. Schiwietz, Radiat. Eff. Defects Solids **112**, 195 (1990).

[8] R. A. Sparrow, R. E. Olsen, and D. Schneider, J. Phys. B **25**, L295 (1992).

[9] D. Schneider, G. Schiwietz, and D. DeWitt, Phys. Rev. A **47**, 3945 (1993); G. Schiwietz, in *Ionization of Solids by Heavy Particles* (Ref. [4]), p. 197.

[10] A. Koyama, T. Shikata, H. Sakairi, and E. Yagi, Jpn. J. Appl. Phys. **21**, 1216 (1982).

[11] J. E. Borovsky and D. M. Suszcynsky, Phys. Rev. A **43**, 1433 (1991); **43**, 1416 (1991).

[12] P. Koschar, K. Kroneberger, A. Clouvas, M. Burkhard, W. Meckbach, O. Heil, J. Kemmler, H. Rothard, K. O. Groeneveld, R. Schramm, and H. D. Betz, Phys. Rev. A **40**, 3632 (1989).

[13] E. J. Sternglass, Phys. Rev. **108**, 1 (1957).

[14] H. Rothard, J. Schou, and K. O. Groeneveld, Phys. Rev. A **45**, 1701 (1992).

[15] N. Bohr and K. Dan. Vidensk. Selsk. Mat. Fys. Medd. **18**, No. 8 (1948), J. Lindhard, and A. Winther, *ibid.* **34**, No. 4 (1964).

[16] H. Rothard, D. Dauvergne, M. Fallavier, K. O. Groeneveld, R. Kirsch, J. C. Poizat, J. Remillieux, and J. P. Thomas, Radiat. Eff. Defects Solids **126**, 373 (1992); in *Ionization of Solids on Heavy Particles* (Ref. [4]), p. 215.

[17] H. P. Beck and R. Langkau, Z. Naturforsch. Teil A **30**, 981 (1975).

[18] H. Rothard *et al.*, Phys. Rev. A **41**, 2521 (1990).

[19] The integration of Eq. (4) of Ref. [11] leads to a − sign in the last bracket of Eq. (7) of Ref. [11], and not a + sign.

[20] B. Gervais and S. Bouffard, Nucl. Instrum. Methods Phys. Res. Sect. B **88**, 355 (1994).

[21] G. S. Khandelwal and E. Merzbacher, Phys. Rev. **151**, 12 (1966); At. Data **1**, 103 (1969).

[22] J. Lindhard, K. Dan. Vidensk. Selsk. Mat. Fys. Medd. **28**, No. 1 (1954).

[23] E. A. Taft and R. H. Philipp, Phys. Rev. **138**, A197 (1965).

[24] K. Kroneberger *et al.*, Nucl. Instrum. Methods Phys. Res. Sect. B **29**, 621 (1988).

[25] H. Rothard *et al.*, Phys. Rev. B **41**, 3959 (1990); in *Ionization of Solids by Heavy Particles,* (Ref. [4]), p. 215.

[26] M. Burkhard *et al.*, J. Phys. D **21**, 472 (1988); H. Rothard, M. Schosnig, K. Kroneberger, and K. O. Groeneveld, in *Interaction of Charged Particles with Solids and Surfaces,* Vol. 271 of *NATO Advanced Study Institute, Series B: Physics,* edited by A. Gras-Marti, H. M. Urbassek, N. Arista, and F. Flores (Plenum, New York, 1991), p. 615.

[27] C. R. Shi, H. S. Toh, D. Lo, R. P. Livi, M. H. Mendenhall, D. Z. Zang, and T. H. Tombrello, Nucl. Instrum. Methods Phys. Res. Sect. **9**, 263 (1985).

[28] M. J. Gaillard, J. C. Poizat, A. Ratkowski, J. Remillieux, and M. Auzas, Phys. Rev. A **16**, 2323 (1977).

[29] R. Latz, Ph. D. thesis, J. W. Goethe University, Frankfurt am Main, Germany, 1984.

[30] A. Clouvas *et al.*, Phys. Rev. B **43**, 2496 (1991); **48**, 6832 (1993).

[31] R. Bimbot, Nucl. Instrum. Methods Phys. Res. Sect. B **69**, 1 (1992).

[32] I. L. Shinpaugh, W. Wolff, H. E. Wolff, U. Ramm, O. Jagutzki, H. Schmidt-Böcking, J. Wang, and R. E. Olson, J. Phys. B **26**, 2869 (1993).

[33] Ch. Tomaschko *et al.*, Nucl. Instrum. Methods Phys. Res. Sect. B **88**, 6 (1994); K. Boussofiane-Baudin *et al.*, *ibid.* **88**, 61 (1994).